Design and development of the magnetic diagnostic systems for the first operational phase of the SMART tokamak

F. Puentes-del Pozo,[1] P. Vicente-Torres,[1] D. J. Cruz-Zabala,[1] S. Munaretto,[2] M. Garcia-Munoz,[1] E. Viezzer,[1] A. Mancini,[1] A. Rodriguez-Gonzalez,[1] J. Sanchez-Gamino,[1] and J. Segado-Fernandez[1]
[1)]*Department of Atomic, Molecular and Nuclear Physics, University of Seville, Seville, 41012, Spain*
[2)]*Princeton Plasma Physics Laboratory, Princeton, NJ 08540, USA.*

(*fpuentes@us.es)

(Dated: 22 July 2024)

A set of magnetic diagnostics has been designed, manufactured and calibrated for the first operational phase of the SMall Aspect Ratio Tokamak (SMART). The sensor suite is comprised of Rogowski coils, 2D magnetic probes, and poloidal, saddle, and diamagnetic flux loops. A set of continuous Rogowski coils has been manufactured for the measurement of plasma current and induced eddy currents in conductive elements. A set of flux loops and magnetic probes will be used as input for the reconstruction of the magnetohydrodynamic (MHD) equilibrium. The quantity and position of these sensors have been verified to be sufficient with synthetic equilibrium reconstructions using the Equilibrium FITting (EFIT) code and baseline scenarios computed with the Fiesta code. These sensors will also be used as input for the real-time control system and magnetic probes will be used for the detection of plasma instabilities. The calibration procedure of the magnetic probes is described and the results are shown. The signal conditioning and data acquisition systems are described.

I. INTRODUCTION

Magnetic diagnostics are one of the basic diagnostics in tokamaks and are present in all machines as they are essential for their operation. These sensors measure magnetic fields and fluxes created by the plasma and the coil system, which can be used to reconstruct the magnetohydrodynamic (MHD) equilibrium fields, to detect instabilities in the plasma, and as input for the real-time (RT) control of the device[1].

The SMall Aspect Ratio Tokamak (SMART) is a spherical tokamak (ST) that is currently being commissioned at the University of Seville (FIG. 1). SMART has been designed with flexible shaping capabilities, allowing for plasmas with both positive tringularity (PT) and negative tringularity (NT)[2–4]. The main objective of SMART is to experimentally validate the combination of ST with NT plasmas as an alternative concept for fusion power plants. To achieve this SMART will have three development phases of increasing toroidal field, plasma current, external heating, and pulse length[5].

ST are characterized by having a reduced aspect ratio, that is, the ratio between the major and minor radius of the plasma torus, which results in a compact design. As the toroidal field created by the toroidal field coils in a tokamak decreases with the mayor radius, the reduced aspect ratio in ST takes better advantage of this field, achieving enhanced values of β_{pol} and a more efficient confinement[6]. But ST come with some disadvantages, as the compact design also reduces the available area for the central solenoid, reducing the flux swing of the machine, and also focuses the divertor region on a smaller area, increasing the power exhaust requirements in the divertor.

On the other hand, NT plasmas have been shown to have confinement capabilities comparable to PT H-mode plasmas[7] while preventing excitation of edge localized modes (ELMs)[8]. Additionally, the geometry of NT plasmas increases the available space in the high field side (HFS), leaving more space for the central solenoid. Furthermore, this geometry places the divertor region at a greater radius, distributing the power flux over a greater area. Thus, NT plasmas can alleviate some of the drawbacks of ST, making this combination attractive for a fusion power plant.

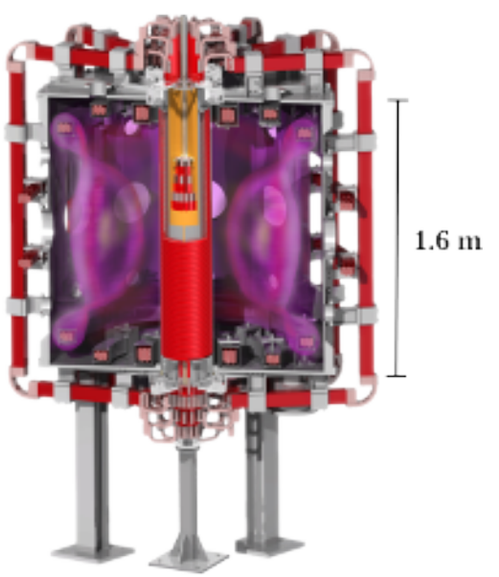

FIG. 1: Rendering of the cross section of SMART (J. Segado-Fernandez et al., Fusion Engineering and Design, Vol. 193, August 2023, 113832; licensed under a Creative Commons Attribution (CC BY) license).

The objective of this work is the design and development of the magnetic sensor suite that will be used during the first operational phase of SMART and is structured as follows. In section II the working principles of magnetic diagnostics are explained, in section III the design of the sensor suite and the sensors themselves are described, in section IV this design is validated using synthetic signals, in section V the calibration of the magnetic probes is shown, and in section VI the conclusions of this work are discussed.

II. BASICS ON MAGNETIC DIAGNOSTICS

Due to the harsh conditions inside a tokamak, inductive sensors are the most commonly used, as they are more robust and reliable than semiconductor-based sensors[1]. Inductive sensors are based on Faraday's law of induction:

$$V = -\frac{d\Phi_B}{dt}, \tag{1}$$

where V is the voltage induced and Φ_B is the magnetic flux through the sensor. This implies that the signal might need to be integrated to obtain the measurement. Depending on the geometry of the coil, different magnetic quantities can be measured.

A loop of wire following a closed path can be used to measure the magnetic flux through the enclosed surface. If this loop is placed at a given poloidal location along a toroidal turn, it is denominated a poloidal flux loop and can be used to measure the poloidal flux, ψ. If located at a given toroidal location along a poloidal turn, it is denominated a diamagnetic loop and can be used to measure the toroidal flux, related with the diamagnetism of the plasma and its stored magnetic energy. Finally, if this loop is installed forming a square along certain poloidal and toroidal angles in the vacuum vessel walls, it is denominated a saddle loop and can be used to measure the radial flux and poloidal flux differences.

Electromagnetic quantities are also measured with compact coils of wire. A small coil can be used to measure the local component of the magnetic field along the coil axis by assuming the magnetic field to be approximately uniform inside it. These coils are often referred to as magnetic probes or Mirnov coils and their reduced size also will result in a greater bandwidth which will allow for measurement of high frequency fluctuations of the fields created by instabilities in the plasma. The bandwidth of these sensors will be limited by the resonance of the RLC circuit created by the self-inductance of the coil and the resistance and parasitic capacitance of the wires. The signal of these sensors from an external field, B_{ext}, that oscillates at a frequency, ν, will be given by:

$$\begin{aligned} V_{Mir} &= -NA\frac{dB}{dt} = \\ &= -\int H(\nu)B_{ext}(\nu)e^{i2\pi\nu t}d\nu \xrightarrow{\nu \ll \nu_{res}} -NAB_{ext}2\pi\nu, \end{aligned} \tag{2}$$

where N is the number of turns of the coil, A its transversal area, H is the sensor transfer function that describes its frequency response, and ν_{res} is the resonance frequency of the sensor.

Finally, an elongated coil that follows a closed path can be used to measure the line integral of the magnetic field, which is related to the enclosed current, I, through Ampere's law by:

$$V_{Rog} = -\mu_0 nA\frac{dI}{dt}, \tag{3}$$

where μ_0 is the vacuum permeability, n the number of turns per unit of length of the coil, and A its transversal area. An additional return wire is passed through the center of the coil to remove the contribution of the magnetic flux through the enclosed surface. These coils are often denominated Rogowski coils and can be used to measure the plasma current, I_p, and the induced eddy currents in the conductive structures of the machine without coming into contact with them.

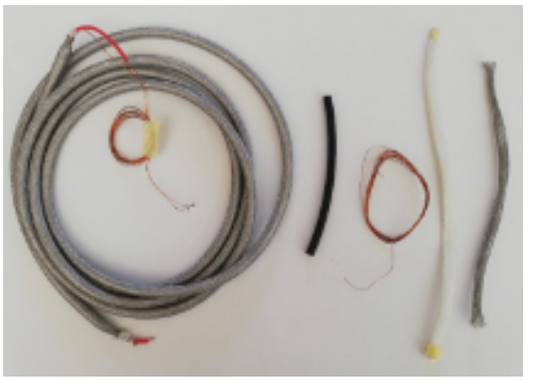

FIG. 2: Rogowski coil for SMART. From left to right, a section of coil, flexible viton former of 6 mm in diameter, Kapton insulated copper wire of 0.3mm in diameter, glass fiber insulating sheath and constatan shielding screen.

III. SENSOR SUITE DESIGN

A. Rogowski coils.

To improve SMART shaping capabilities, the vacuum vessel has been designed with a rectangular poloidal cross section and in-vessel poloidal field coils installed inside conductive casings[9]. The vacuum vessel is built with low resistivity and without electrical breaks, so the induced toroidal eddy currents will be significant and should be measured. To perform these measurements, a set of 10 Rogowski coils will be installed on SMART. Two of them, for redundancy, will be installed outside the vacuum vessel, two of them will be installed inside of the vessel along the vacuum vessel walls, and the remainder will be installed one around each of the in-vessel poloidal field coils. This configuration allows for simple measurement of the plasma current by subtracting the signals of the casing Rogowski coils from the internal one and of the vessel eddy currents by subtracting the signal of the internal Rogowski coil from the external. The eddy currents in the casings can also be measured by subtracting the currents measured in the power supplies from the casing Rogowski coils measurements.

The Rogowski coil set for SMART has been designed with a flexible viton former that allows the coil to bend around the vacuum vessel walls and the in-vessel coil casings, permitting the use of continuous coils. In FIG. 2, a section of this coil can be seen along with samples of the materials used to manufacture it. A viton tube is used as the former for the coil, around which Kapton-insulated copper wire is wound at 3000 turns/m. A sheath of glass fiber is placed around the coil to provide additional electrical insulation and a constatan screen is used as shielding. An additional return wire is passed through the center of the coil to be used as a diamagnetic loop.

B. Magnetic probes

A set of 2D magnetic probes has been commissioned for SMART to measure the equilibrium fields as input for the equilibrium reconstruction and for the detection of high frequency instabilities. In order to have enough sensitivity for the

FIG. 3: 2D magnetic probe for SMART. The sensor is 25 x 25 x 15 mm in size and is wound using Kapton insulated copper wire of 0.4 mm in diameter on a Macor former.

equilibrium measurements while maintaining enough bandwidth for the instability measurements, these coils have been designed with a compromise between the effective area *NA*, and bandwidth while complying with the space constraints inside of the vacuum vessel. These probes will be installed along the vacuum vessel walls aligned as to measure the components of the poloidal magnetic field, tangential and orthogonal to the wall. In FIG. 3, one of these probes can be seen. The coils are manufactured manually with a Macor former and Kapton insulated copper wire that was densely wound to ensure good axis alignment and prevent vibrations. A poloidal array of 16 of these coils is installed for equilibrium measurements and a toroidal array of 4 coils placed in the low field side (LFS) mid-plane is installed for instability measurements.

C. Flux loops

A set of 30 poloidal flux loops are installed at different poloidal positions, with 6 of them installed in the in-vessel coil casings and the rest along the vacuum vessel walls. These sensors will be used for measurements of the equilibrium poloidal flux and one-turn voltage. They will also be used as input for the RT control feedback loop, and therefore they will be installed inside of the vacuum vessel to avoid the delay of the fields through the vacuum vessel walls. The flux loop in the HFS midplane will be used as the reference loop, and the rest of flux loop signals will be referenced to it. Additionally, a set of 8 saddle loops are installed along the LFS midplane to provide measurements of poloidal flux in positions where a full flux loop can not be installed due to the large rectangular ports of the vessel. They will also measure toroidal asymmetries in the radial field and slow-rotating toroidal modes with frequencies of up to a few kHz given the 0.1 ms resistive timescale of the LFS vacuum vessel wall. These saddle loops are attached to the outside of the vacuum vessel. The complete layout of the magnetic diagnostic suite, showing the positions of the sensors along the vessel walls, can be seen in FIG. 4.

D. Signal conditioning and data acquisition

The signals from all the in-vessel sensors will be carried out of the vessel using twisted pair Kapton-insulated copper

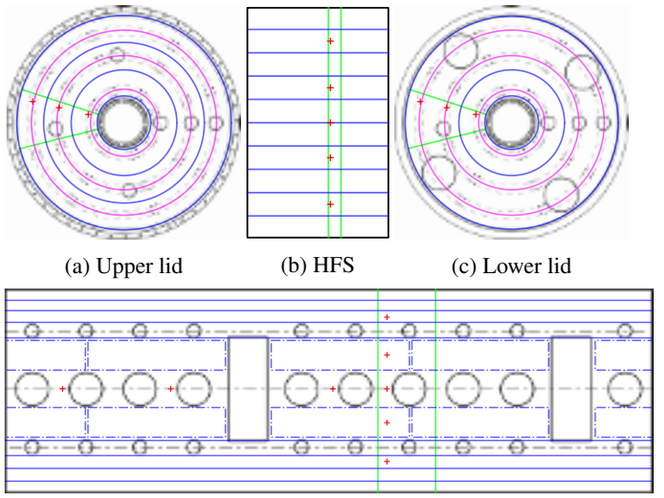

(a) Upper lid (b) HFS (c) Lower lid

(d) LFS

FIG. 4: Distribution of sensors along the (a) upper lid, (b) high field side, (c) lower lid and (d) low field side of the vacuum vessel walls. Rogowski coils are represented with green lines, flux loops in the walls with blue lines, flux loops in the poloidal coil casings with magenta lines, saddle loops with dashed blue lines, and magnetic probes with red crosses.

wire to bring the signals to an electrical vacuum feed-through which is insulated from the vessel. These differential signals in conjunction with the ones from the out of vessel sensors will then be transported with a twisted pair double-grounded-screened cable to a signal conditioning printed circuit board. This board has been designed to be configurable and modular and will perform a series of analog operations on the differential signals, including overvoltage protection, signal amplitude attenuation, signal integration, and arithmetic operations between signals. The attenuation factor can be manually modified to better optimize the input voltage range of the data acquisition (DAQ) system.

The analog arithmetic operations are configurable and will be used to perform reference signal subtraction and calculation of flux differences and plasma current for input to the RT control system. The boards will also count with a 300 kHz 4^{th} order Butterworth low-pass filter for anti-aliasing and to reduce the noise induced by the switched power supplies of the shaping coils[2]. The signals will be digitized by a NI PXIe-6375 DAQ module at 1 Msample / s / channel with a 16 bit resolution with a variable input range $\pm$ 0.1 - 10 V. This module shares a controller with the power supply control module to facilitate the implementation of the RT control system.

IV. SYNTHETIC DIAGNOSTIC STUDY

To validate the design of the magnetic diagnostic suite for SMART, synthetic signals from multiple sensors were simulated. To do so, baseline scenarios of PT and NT have been simulated for the first operational phase of SMART using the Fiesta code[10], which provides both the flat-top equilibrium and the current waveform in the coils, plasma, and conductive structures. The current waveforms were used to calculate

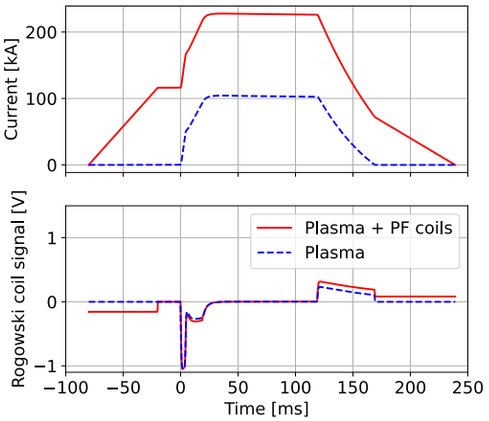

FIG. 5: Current waveforms for a SMART first phase baseline scenario calculated with FIESTA and the corresponding synthetic signal expected from the Rogowski coil installed inside of the vacuum vessel.

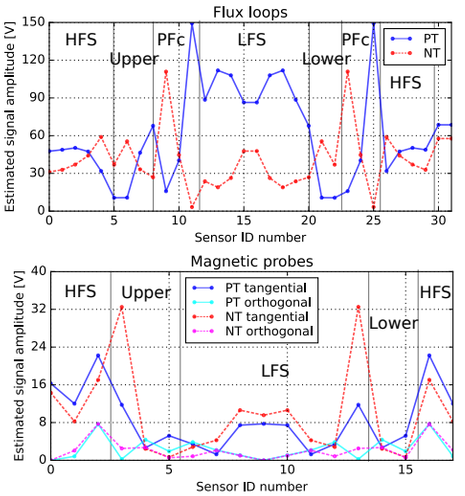

FIG. 6: Maximum signal amplitude expected for each flux loop and magnetic probe in the case of a current quench disruption in the first phase of SMART. Sensors are numbered starting from the HFS midplane increasing in the clockwise direction.

the synthetic signal of the interior Rogowski coil, which can be seen in FIG. 5.

The flat-top equilibrium has been used to estimate the maximum signal amplitude that is expected from flux loops and magnetic probes in the case of a fast disruption by interpolating the equilibrium fields at the sensor positions. This estimation was done supposing a current quench disruption where the plasma current rapidly goes to zero from the flat top due to a loss of confinement. The time scale for this type of disruption given the vacuum vessel parameters of SMART was determined to be around 0.5 ms in a previous work[11]. The estimated amplitudes can be seen in FIG. 6 and will be used to determine the signal attenuation required to avoid DAQ saturation and the consequent loss of information in this event.

To validate the reliability of the sensor suite for the reconstruction of MHD equilibrium, baseline scenarios were sampled at the sensors' positions and used as input for the Equilibrium FITting (EFIT) code, which computes the equilibrium reconstruction[12]. The measurement uncertainty of the synthetic measurements was quantified by their bit equivalent, that is, the change in measured quantity equivalent to a change of 1 bit in the DAQ system. This quantity has been estimated from the predicted signal amplitudes in FIG. 6 by determining for each signal the attenuation and DAQ input range that avoids saturation while best utilizing available the input range to maximize the resolution. Then, the bit equivalent can be calculated using geometrical parameters in the case of flux loops and the calibrations of Sec. V in the case of the magnetic probes to obtain the proportionality between voltage and measured quantity. Magnetic probes have been treated as point measurements for simplicity, but their finite size will introduce small deviations that will be taken into account in the future.

The reference and reconstructed equilibria for the PT and NT baseline scenarios can be seen in FIG. 7 along with the normalized reconstruction error. The greatest error in the reconstruction is located close to the magnetic axis, as is expected from the literature, as is the point farthest away

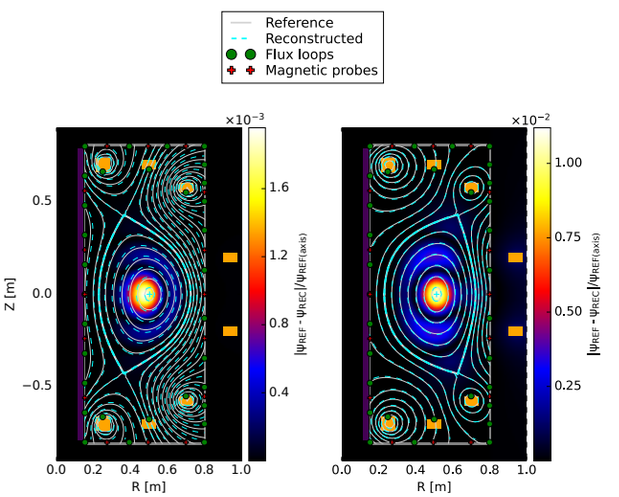

FIG. 7: Synthetic equilibrium reconstruction of the first operational phase baseline scenarios in SMART. The colormap shows the reconstruction error normalized to the poloidal flux on the magnetic axis of the reference equilibrium.

from the sensors, and the extrapolation error increases with distance[1].

To ensure that the sensor suite will be capable of performing equilibrium reconstructions during a complete experimental campaign, even if some sensors are damaged and become unreliable, a simultaneous sensor failure robustness study has been carried out. To do so, 30 sets of 200 equilibrium reconstructions are performed, but before each of the reconstructions, a certain amount of randomly selected sensors are disabled by setting their fitting weights to 0, with the number of disabled sensors increasing in each set of reconstructions. Then, if the normalized reconstruction error is less than 3%

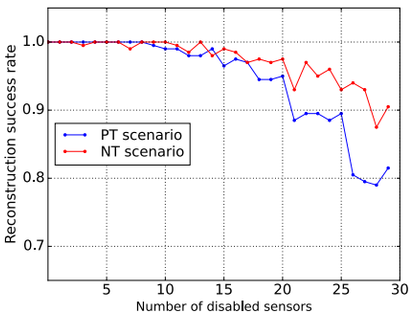

FIG. 8: Success rate of the synthetic equilibrium reconstructions in the case of multiple simultaneous sensor failure.

at all points in the simulation grid, the reconstruction is considered successful. The results of this study can be seen in FIG. 8, which shows that successful reconstructions can be achieved in more than 90% cases with up to 25 of the 70 total sensors simultaneously disabled for the PT and NT baseline scenarios.

V. MAGNETIC PROBE CALIBRATION

An out of vessel calibration of the magnetic probes with a frequency sweep of 100 to 10^7 Hz was performed prior to the installation of the diagnostic suite to determine their effective area and frequency response. For each frequency a sinusoidal external magnetic field of that frequency was applied to the sensor with a waveform generator and an external solenoid or Helmholtz coil pair, depending on the frequency. The magnetic field was determined using a shunt resistor to measure the current in the external coil, and the probe signal and the shunt voltage were recorded using an oscilloscope. Both signals were fitted with a sine to determine their amplitudes, with the response of the coil determined by the coefficient of the two amplitudes[13]. This sweep was divided into three to reduce the raw file size while maintaining a sample rate of more than 10 times the maximum frequency and at least 10 oscillations for each frequency throughout each sweep. This also allows to adapt the experimental setup to the most optimal for the frequency range.

From 100 to 1000 Hz the sweep was performed using a long solenoid and a 10 W amplifier. A linear regression between probe response and field frequency in this range was performed to determine the effective area. From 1 kHz to 100 kHz the sweep was performed with a set of Helmholtz coils, as they offer less input impedance at high frequencies than the solenoid. From 0.1 to 10 MHz the amplifier was removed to prevent signal distortion, and the waveform generator was connected directly to the Helmholtz coils. The calibrated frequency response of one of the magnetic probes can be seen in FIG. 9 for both coils of the 2D probe, which exhibits a behavior consistent with the expected RLC resonant circuit. The calibrated effective area and bandwidth of all the magnetic probes can be seen in FIG. 10, which are satisfactorily homogeneous. This figure also illustrates the design trade-off between effective area and bandwidth for inductive sensors.

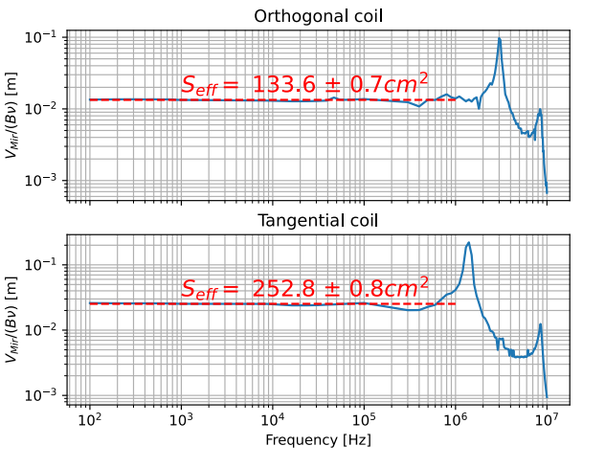

FIG. 9: Calibration of the effective area and frequency response of a 2D magnetic probe.

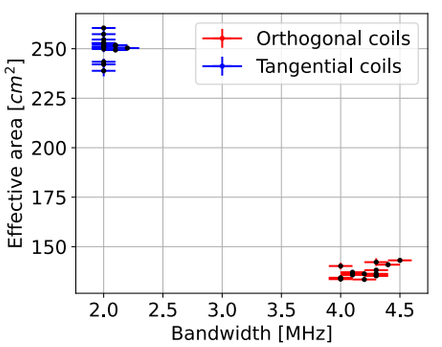

FIG. 10: Calibrated effective area and bandwidth of the 2D magnetic probe array.

VI. CONCLUSION AND OUTLOOK

In this work, the magnetic sensor suite for the first operational phase of SMART consisting of Rogowski coils, 2D magnetic probes and poloidal, diamagnetic and saddle loops has been designed and commissioned. The sensors have been described, their positions in the vessel shown. The reliability of the sensor suite design has been validated through synthetic diagnostics and equilibrium reconstructions. Finally, the magnetic probes have been characterized with an out of vessel calibration. Following the installation of this diagnostic suite, a campaign of vacuum shots will be performed to conclude the calibration of the sensors and the suite as a whole in preparation for the first plasma in SMART.

ACKNOWLEDGMENTS

The support from the European Research Council (ERC) under the European Union's Horizon 2020 research and innovation program (grant agreement No. 805162) is gratefully acknowledged.

This material is based upon work supported by the US De-

partment of Energy, Office of Science, Office of Fusion Energy Sciences, under Awards DE-AC02-09CH11466.

Part of the data analysis was performed using the OMFIT integrated modeling framework[14]

The data that support the findings of this study are available from the corresponding author upon reasonable request.

[1]I. H. Hutchinson, *Principles of plasma diagnostics*, second edition ed. (New York, Melbourne [u.a.], Cambridge, 2005).
[2]M. Agredano *et al.*, Fusion Engineering and Design **168**, 112683 (2021).
[3]S. J. Doyle *et al.*, Fusion Engineering and Design **171**, 112706 (2021).
[4]J. Segado *et al.*, Fusion Engineering and Design **193**, 113832 (2023).
[5]M. Podestà *et al.*, Plasma Physics and Controlled Fusion **66**, 045021 (2024).
[6]Y.-K. Peng and D. Strickler, Nuclear Fusion **26**, 769 (1986).
[7]F. Wagner *et al.*, Physical Review Letters **49**, 1408 (1982).
[8]A. Marinoni *et al.*, Nuclear Fusion **61**, 116010 (2021).
[9]A. Mancini *et al.*, Fusion Engineering and Design **171**, 112542 (2021).
[10]G. Cunningham, Fusion Engineering and Design **88**, 3238 (2013).
[11]A. Mancini *et al.*, IEEE Transactions on Plasma Science **50**, 4187 (2022).
[12]L. Lao *et al.*, Nuclear Fusion **25**, 1611 (1985).
[13]A. Torres *et al.*, Fusion Engineering and Design **168**, 112467 (2021).
[14]O. Meneghini *et al.*, Nuclear Fusion **55**, 083008 (2015).